

**Electronic and dynamical properties of the silicon trivacancy**

J. Coutinho\*

*I3N, Department of Physics, University of Aveiro, Campus Santiago, PT-3810-193 Aveiro, Portugal*

V. P. Markevich, A. R. Peaker, and B. Hamilton

*Photon Science Institute, University of Manchester, Manchester M13 9PL, United Kingdom*

S. B. Lastovskii and L. I. Murin

*Scientific-Practical Materials Research Center of NAS of Belarus, BY-Minsk 220072, Belarus*

B. J. Svensson

*Department of Physics, Oslo University, NO-0316 Oslo, Norway*

M. J. Rayson

*Department of Engineering Sciences and Mathematics, Luleå University of Technology, SE-Luleå S-97187, Sweden*

P. R. Briddon

*School of Electrical, Electronic and Computer Engineering, Newcastle University, Newcastle Upon Tyne NE1 7RU, United Kingdom*

(Received 5 July 2012; published 1 November 2012)

The trivacancy ( $V_3$ ) in silicon has been recently shown to be a bistable center in the neutral charge state, with a fourfold-coordinated configuration,  $V_3$ [FFC], lower in energy than the (110) planar one [V. P. Markevich *et al.*, *Phys. Rev. B* **80**, 235207 (2009)]. Transformations of the  $V_3$  defect between different configurations, its diffusion, and disappearance upon isochronal and isothermal annealing of electron-irradiated Si:O crystals are reported from joint deep level transient spectroscopy measurements and first-principles density-functional calculations. Activation energies and respective mechanisms for  $V_3$  transformation from the (110) planar configuration to the fourfold-coordinated structure have been determined. The annealing studies demonstrate that  $V_3$  is mobile in Si at  $T > 200$  °C and in oxygen-rich material can be trapped by interstitial oxygen atoms so resulting in the appearance of  $V_3O$  complexes. The calculations suggest that  $V_3$  motion takes place via consecutive FFC/planar transformation steps. The activation energy for the long-range diffusion of the  $V_3$  center has been derived and agrees with atomic motion barrier from the calculations.

DOI: [10.1103/PhysRevB.86.174101](https://doi.org/10.1103/PhysRevB.86.174101)

PACS number(s): 61.72.jd, 61.72.Bb, 61.80.Fe, 71.55.Cn

**I. INTRODUCTION**

The lifetime of silicon detectors under intense hadronic radiation is limited by the damage produced, usually in the form of vacancies, interstitials, related aggregates, and higher order defects. Such detectors are widely used to provide particle detection and their spatial distribution in a wide variety of applications, ranging from high energy physics experiments to medical imaging. The detector degradation manifests itself as an increase of the leakage current, free carrier removal, and a decrease of the charge collection efficiency, making radiation tolerance of Si detectors an issue of great concern to which a large effort has been devoted in the last decade (see, e.g., Ref. 1 and references therein).

Considerable interest in silicon vacancies also stems from their capability in limiting transient enhanced diffusion of dopants, as well as for metal gettering purposes. In the first case they are deliberately produced close to shallow dopant implants to reduce the concentration of detrimental Si interstitials,<sup>2</sup> while in the second case they are used to keep metallic contamination away from device active regions by trapping metal atoms at their inner surfaces.<sup>3</sup>

Definitive identification of vacancy defects in Si (i.e., the connection between physical models and their electrical, optical, and magnetic observable properties), as well as

formation and annealing behavior, have only been achieved for the single vacancy (V) and divacancy ( $V_2$ ) defects. Other small  $V_n$  aggregates with  $3 \leq n \leq 6$  have been studied to a lesser extent.<sup>4–16</sup> Some electron spin resonance (ESR) signals in neutron-irradiated Si crystals (particularly A3, A4, P3, and P1), were assigned to different configurations of the  $V_3$ ,  $V_4$ , and  $V_5$  defects.<sup>4–8</sup> However, *ab initio* modeling reports showed that those configurations could not be minimum energy structures for the supposed vacancy clusters. Early density-functional theory (DFT) and Hartree-Fock calculations by Hastings *et al.*<sup>12</sup> indicated that the lowest energy structures for the small vacancy clusters were those obtained by sequential removal of host atoms from the hexagonal ring in the Si lattice. These are referred to as part of hexagonal ring (PHR) structures, and the main argument behind their stability was the minimization of dangling bonds in such defects.<sup>13</sup> However, based on similar dangling bond minimization arguments, DFT studies by Makhov and Lewis<sup>14</sup> have suggested that more stable structures could be obtained for  $V_5$ ,  $V_4$ , and  $V_3$  by successive passivation of up to three groups of four dangling bonds in a hexavacancy by placing one, two, and three extra Si atoms, respectively, at stable interstitial sites edging the  $V_6$  defect (see Fig. 1 from Ref. 14). These complexes comprise a family of fourfold-coordinated (FFC) vacancy defects.

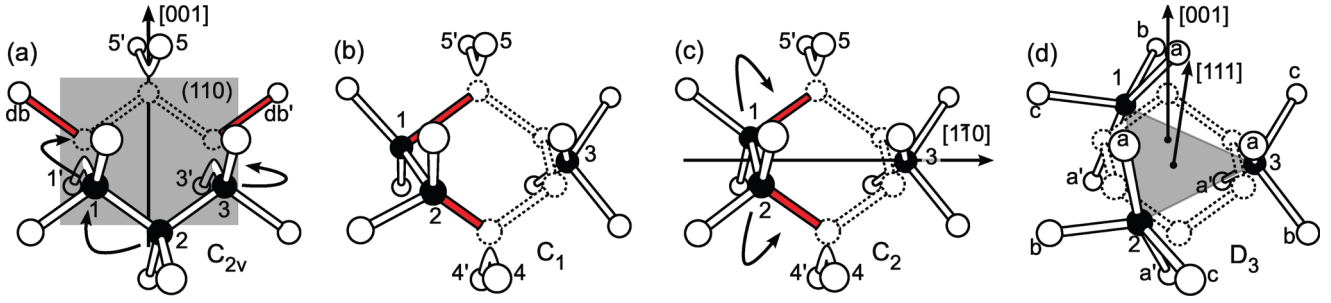


FIG. 1. (Color online) Atomic structure of stable and metastable  $V_3$  complexes in silicon along with high symmetry crystallographic directions and planes. The  $\text{PHR} \rightarrow \text{FFC}$  transformation mechanism is depicted by the arrows indicating the motion of three core Si atoms (1, 2, and 3) from substitutional sites in  $V_3[\text{PHR}]$  (a) to interstitial sites in  $V_3[\text{FFC}]$  (d). These are shown in black for a better perception of their placement with respect to the vacant sites (drawn with a dashed line). Intermediate structures along the mechanism are shown in (b) and (c). Broken bonds are shown as solid sticks (red sticks in the online version), reconstructed radical pairs  $\text{Si}_i\text{-Si}_{i'}$  are shown as “banana” bonds, and Si atoms that are slightly perturbed (or unperturbed) from their lattice sites are shown in white.

Recently, a combined deep level transient spectroscopy (DLTS) and DFT modeling study confirmed that the  $V_3$  defect is a bistable center in the neutral charge state, with a fourfold-coordinated configuration,  $V_3[\text{FFC}^0]$ , lower in energy than the PHR structure,  $V_3[\text{PHR}^0]$ , where all vacant sites lie on a (110) crystalline plane.<sup>15</sup> However, the (110) planar configuration was also found to be the lowest energy structure for the charged  $V_3$  defect.<sup>15,16</sup> The PHR and FFC configurations of  $V_3$  in Si can be seen in Figs. 1(a) and 1(d), respectively.  $V_3[\text{PHR}]$  gives rise to two acceptor levels at 0.36 and 0.46 eV below the conduction band edge ( $E_c$ ) and to two donor levels at 0.19 and 0.11 eV above the valence band edge ( $E_v$ ), while in the FFC configuration it only has an acceptor level at  $E_c - 0.075$  eV. Five signals observed in the DLTS spectra of electron-irradiated Si diodes were associated with charge carrier emission from the above levels.<sup>15,16</sup> It should be mentioned that immediately after electron irradiations, only DLTS signals due to the  $V_3$  defect in the (110) planar configuration were detected. However, storage for a few weeks of the irradiated Si samples at room temperature or shorter anneals in the temperature range 50–100 °C resulted in the transformation of  $V_3$  from the PHR configuration into the most stable  $V_3[\text{FFC}]$ . The defect could be restored to the metastable planar configuration by application of forward bias injection with a current density in the range 10–15 A/cm<sup>2</sup> for 10–20 min at about 300 K. The above transformations between the FFC and PHR configurations were found to be fully reversible in both the electron-irradiated *n*- and *p*-type Si samples.<sup>15,16</sup>

It was reported in Refs. 15 and 16 that 30-min isochronal annealing of the irradiated  $p^+-n$  and  $n^+-p$  diodes in the temperature range 200–275 °C resulted in the disappearance of the levels due to  $V_3$  and to the correlated appearance of a defect with two acceptor levels at 0.34 and 0.455 eV below  $E_c$  and to two donor levels at 0.23 and 0.12 eV above  $E_v$ . It was argued that the disappearance of  $V_3$  upon annealing at temperatures above 200 °C could be associated with its diffusion and interaction with interstitial oxygen, the most abundant impurity in the samples studied. The above four levels were tentatively assigned to the  $V_3\text{O}$  complex.<sup>15–17</sup>

The  $V_3$  defect is one of the principal defects responsible for the degradation of silicon detectors and bipolar transistors upon irradiation with high energy particles,<sup>11,18,19</sup> and so,

understanding the details of its electronic structure and dynamic properties will help in developing defect engineering methods for improving the radiation tolerance of the Si-based devices. Despite the considerable achievements towards the identification and characterization of the trivacancy in Si, several questions are still unresolved. For instance, any successful defect model will have to account for the  $\sim 1$  eV thermally activated barrier for the transformation of  $V_3$  from the (110) planar configuration into the FFC one in the temperature range 30–120 °C, as well as to explain how the  $V_3$  defect anneals out in the temperature range 200–300 °C. In the present work we address these issues by reporting on the annealing kinetics of the DLTS signals associated with the energy levels of the trivacancy and the derived activation energies for transformations and migration of the defect. These reports are accompanied with density-functional theoretical calculations of the mechanisms related to these transformation and migration processes. The paper is divided as follows: In Secs. II and III we provide the details of the experimental techniques and sample preparation, as well as the theoretical methods for the modeling studies. In Secs. IV and V we report on the experimental and theoretical results, respectively, and finally we present our conclusions in Sec. VI.

## II. EXPERIMENTAL METHODS AND SAMPLE PREPARATION

Experimental results in the present work were obtained from DLTS and high-resolution Laplace DLTS (L-DLTS)<sup>20</sup> measurements on electron-irradiated  $p^+-n-n^+$  ( $n^+-p-p^+$ ) diodes and on bare Si samples on which Schottky barrier diodes were prepared after electron irradiations. The  $p^+-n-n^+$  diodes were formed by implantation and subsequent thermal activation of boron ions into phosphorus-doped ( $\rho \approx 30 \Omega \text{ cm}$ ) epi-Si grown on highly Sb-doped bulk Czochralski-grown (Cz) Si wafers. The  $n^+-p-p^+$  diodes were produced on boron-doped epi-Si ( $\rho \approx 20 \Omega \text{ cm}$ ), which was grown on highly boron-doped Cz-Si wafers. The diodes were formed by implantation of phosphorus ions with subsequent annealing at 1150 °C in nitrogen-oxygen gas ambient. Oxygen concentrations in the epi-layers were determined from the rate of transformation of  $V_2$  to the divacancy-oxygen defect with the

use of data presented in Ref. 21. The oxygen concentration was in the range  $(3-4) \times 10^{17} \text{ cm}^{-3}$  in all the epi-Si samples. Gold Schottky barrier diodes were prepared on samples from an  $n$ -type Si crystal with an initial resistivity of  $5 \text{ } \Omega \text{ cm}$ , which was grown by the Czochralski method. Concentrations of interstitial oxygen and substitutional carbon atoms in these samples were measured by optical absorption at room temperature. The oxygen concentration was about  $(9-10) \times 10^{17} \text{ cm}^{-3}$  and the carbon concentration was below the detection limit of  $2 \times 10^{15} \text{ cm}^{-3}$ .

All the samples were irradiated with either 4- or 6-MeV electrons at room temperature with the use of a linear accelerator. The flux of electrons was  $1 \times 10^{12} \text{ cm}^{-2} \text{ s}^{-1}$ .

Forward-bias injection and thermal-annealing treatments of the irradiated structures at temperatures lower than 400 K were carried in a He-closed-cycle cryostat in vacuum. Thermal anneals of the samples in the temperature range 150–350 °C were carried out in a furnace in a dry  $\text{N}_2$  ambient.

Concentrations of trivacancy in the PHR and FFC configurations in  $p^+-n-n^+$  structures and Schottky diodes were determined from the magnitudes of capacitance changes due to  $\text{V}_3[\text{PHR}](=/-)$  and  $\text{V}_3[\text{FFC}](-/0)$  transitions measured with Laplace DLTS in the temperature ranges 160–170 K and 40–50 K, respectively. Concentration of the  $\text{V}_3[\text{PHR}]$  configuration in  $n^+-p-p^+$  structures was determined from the magnitudes of capacitance changes due to the  $\text{V}_3[\text{PHR}](++/+)$  transition measured with L-DLTS in the temperature range 60–70 K.

### III. THEORETICAL METHOD

Electronic structure calculations were carried out using a density-functional code (AIMPRO),<sup>22,23</sup> along with the local spin density approximation (LSDA) for the exchange and correlation potential.<sup>24</sup> Explicit treatment of  $\text{Si}:1s^2 2s^2 2p^6$  core states was avoided by using the pseudopotentials of Hartwigsen, Goedecker, and Hutter,<sup>25</sup> while valence states were expressed as linear combinations of Cartesian-Gaussian atom centered functions with angular momentum up to  $l = 2$  comprising up to 13 functions per Si atom. Hartree, exchange and correlation terms, as well as the charge density were Fourier transformed using plane waves with a cutoff energy set at  $E_{\text{cut}} = 80 \text{ Ry}$ . These conditions ensured good convergence of energy differences like ionization energies and migration barriers.<sup>26</sup> Using a larger basis set (up to 28 Cartesian-Gaussian functions per atom) resulted in total energy changes of bulk Si by less than 15 meV/Si atom and in ionization energies by less than 0.02 eV.

The host crystal was accounted for by using 512-Si atom cubic supercells, from which three atoms were removed to produce a trivacancy. All atoms were moved along their forces during a conjugate gradient relaxation cycle to minimize the energy. This was carried out until total energy and atom position changes dropped below 0.3 meV and  $5 \times 10^{-5} \text{ } \text{\AA}$ , respectively. The Brillouin zone was sampled at  $\mathbf{k} = \Gamma$ , and under these conditions, the equilibrium lattice parameter and bulk modulus were  $a_0 = 5.3947 \text{ } \text{\AA}$  and  $B = 98.3 \text{ GPa}$ . The Kohn-Sham gap at  $\mathbf{k} = \Gamma$ , excitonic gap and quasiparticle gap energies were  $\epsilon_{\text{KS}} = 0.56 \text{ eV}$ ,  $E_{\text{g,X}} = 1.32 \text{ eV}$ , and  $E_{\text{g,QP}} = A - I = 1.33 \text{ eV}$ , respectively. Here,  $E_{\text{g,X}}$  refers to the energy

needed to promote an electron from the highest occupied state to the lowest unoccupied state at  $\mathbf{k} = \Gamma$ , whereas  $A$  and  $I$  stand for the electron affinity and ionization potential, respectively, calculated from 512-atom bulk charged supercells (properly compensated by a uniform background charge of the opposite sign). The lattice constant and bulk modulus compare well with their respective experimental values,  $a_{0,\text{exp}} = 5.431 \text{ } \text{\AA}$  and  $B_{\text{exp}} = 97.9 \text{ GPa}$ .<sup>27</sup> The one-electron gap is underestimated by roughly 50%, and this is well known to arise from a discontinuity  $\Delta$  in the exchange and correlation potential when the number of electrons is changed.<sup>28</sup> Although the total-energy quasiparticle gap  $E_{\text{g,QP}}$  is very close to the experimental gap of 1.17 eV measured at  $T \approx 0 \text{ K}$ ,<sup>29</sup> we should avoid any misinterpretation of such a coincidence by noting that the calculations were carried out for a periodic system with a size that corresponds to an extremely high density of excitations ( $\sim 10^{20} \text{ cm}^{-3}$ ).<sup>30</sup>

Defect formation energies  $E_{\text{f}}$  are usually calculated under periodic boundary conditions (see Ref. 26 and references therein), with reference to chemical potentials for electrons ( $\mu_e$ ) and atoms ( $\mu_i$ ) whose species  $i$  occur  $n_i$  times in a supercell,

$$E_{\text{f}}[\mathbf{R}^q](\mu_e) = E[\mathbf{R}^q] - \sum_i n_i \mu_i + q(E_v + \mu_e) + \xi[\mathbf{R}^q]. \quad (1)$$

Here  $E[\mathbf{R}^q]$  stands for the total energy of a defective supercell with a defect structure  $\mathbf{R}$  and net electronic charge  $q$  (which relates to an excess or deficit of electrons with respect to the neutral supercell). The electronic chemical potential is given with respect to the valence band top  $E_v$  (i.e., the highest occupied Kohn-Sham energy at  $\mathbf{k} = \Gamma$  from a bulk calculation). The correction  $\xi$  accounts for spurious effects such as any valence band misalignment between bulk and defective supercells, or those arising from the artificial lattice of charged defects that result from the periodic boundary conditions (adequately compensated by a *jellium* background of opposite charge).<sup>31,32</sup>

An electrical level of a defect is defined as the chemical potential  $\mu_e \equiv I(q/q+1) - E_v$  where the crossing of  $E_{\text{f}}[\mathbf{X}^q]$  and  $E_{\text{f}}[\mathbf{Y}^{q+1}]$  takes place, so that the defect will be found at  $q$  and  $q+1$  charge states when  $\mu_e > I(q/q+1) - E_v$  and  $\mu_e < I(q/q+1) - E_v$ , respectively. Note that we distinguish between  $\mathbf{X}^q$  and  $\mathbf{Y}^{q+1}$  structures since these are not necessarily the same after equilibrium is reached upon changing the charge state. Therefore, from Eq. (1) we may write

$$I(q/q+1) = \mathcal{E}[\mathbf{X}^q] - \mathcal{E}[\mathbf{Y}^{q+1}], \quad (2)$$

where  $\mathcal{E}[\mathbf{R}^q] = E[\mathbf{R}^q] + \xi[\mathbf{R}^q]$  is a *corrected* total energy. Unfortunately  $\xi$  is ill defined and usually hard to obtain. First because there is no absolute energy reference when periodic boundary conditions are used,<sup>33</sup> and secondly because multipole interactions in a three-dimensional lattice are long ranged and conditionally convergent.<sup>31</sup> Although these effects can all be estimated, progress can be made by introducing appropriate experimental data. Accordingly, we can compare ionization potentials  $I(q/q+1)$  for the defect under scrutiny (hereafter subscripted with “d”) with that of a defect that is well established experimentally, usually referred to as *marker*

(subscripted with “m”).<sup>26,34,35</sup> The method basically assumes that the offset  $\delta = I_d(q/q+1) - I_m(q/q+1)$  is essentially identical to  $E_d(q/q+1) - E_m(q/q+1)$ , where the latter energies refer to the calculated defect level and experimentally observed marker level, respectively. A further simplification is obtained if we assume that  $I(q/q+1) = E[\mathbf{X}^q] - E[\mathbf{Y}^{q+1}]$ , and hence defect level energies are predicted at

$$E_d(q/q+1) \approx I_d(q/q+1) - I_m(q/q+1) + E_m(q/q+1). \quad (3)$$

The last step makes a bold assumption, and that is that valence band and defect-image interaction corrections ( $\xi$  values) are similar for both the marker and the defect under scrutiny. The error from this assumption is lower the greater the similarity between the localization and shape of the donor (or acceptor) states of both defects. Unfortunately for many defects, no particularly obvious markers are available, and often  $I_m(q/q+1)$  in Eq. (3) is replaced by  $I_{\text{bulk}}(q/q+1)$ , and  $E_m(q/q+1)$  is taken as  $E_v$  or  $E_c$ , for  $q \geq 0$  or  $q < 0$ , respectively, where the subscript “bulk” implies that the calculation is carried out in a defect-free supercell.<sup>36</sup> This particular *flavor* of the marker method is rather appealing as it is parameter free.

Let us now exemplify how level calculations are carried out for the FFC form of  $V_3$  with  $D_3$  symmetry. From total energy calculations of a bulk supercell with 512 Si atoms, we have  $I_{\text{bulk}}(0/+)=5.00$  eV and  $I_{\text{bulk}}(-/0)=6.34$  eV. These values set the location of the valence band top and conduction band bottom energies. Conversely, for  $V_3$ [FFC] we have  $I_d(0/+)=5.01$  eV and  $I_d(-/0)=6.18$  eV. Hence, from Eq. (3), for the donor level we have

$$E_d(0/+) - E_v = I_d(0/+) - I_{\text{bulk}}(0/+) = 0.01 \text{ eV},$$

whereas for the acceptor we obtain

$$E_c - E_d(-/0) = I_{\text{bulk}}(-/0) - I_d(-/0) = 0.16 \text{ eV}.$$

In agreement with the previous reports,<sup>15,37</sup> these results suggest that  $V_3$ [FFC] has an acceptor level just below the conduction band bottom, while any donor activity is unlikely because the ionization energies of defective and bulk supercells are essentially the same.

The marker method is particularly suitable to estimate the energy of electronic transitions like those observed in DLTS or optical experiments. However, we can also make use of it to produce a formation energy diagram, and hence to calculate the relative stability of a particular defect as a function of the electron chemical potential. To this end we define the formation energy  $E_f$  of a neutral defect  $\mathbf{R}_d^0$ ,

$$E_f[\mathbf{R}_d^0] = E[\mathbf{R}_d^0] - \sum_i n_i \mu_i, \quad (4)$$

the formation energy for positive charge states as

$$E_f[\mathbf{R}_d^q](\mu_e) = E_f[\mathbf{R}_d^{q-1}] + q\mu_e - q[I_d(q-1/q) - I_m(q-1/q)], \quad (5)$$

and the analogous quantity for negative charge states as

$$E_f[\mathbf{R}_d^q](\mu_e) = E_f[\mathbf{R}_d^{q+1}] + q\mu_e - q[E_g + I_d(q/q+1) - I_m(q/q+1)], \quad (6)$$

where  $n_i$ ,  $\mu_i$ , and  $\mu_e$  were already introduced in Eq. (1). In the present case, our supercells have a unique chemical species ( $i = \text{Si}$ ),  $n_{\text{Si}} = 509$ , and  $\mu_{\text{Si}}$  is the energy per Si atom taken from a bulk Si calculation with 512 atoms. We also note that for negative charge states a band gap energy  $E_g$  has been introduced. This should be the experimental gap when  $I_m(q/q+1)$  is calculated for a marker defect, or alternatively could be replaced by  $E_{g,\text{QP}} = I_{\text{bulk}}(-/0) - I_{\text{bulk}}(0/+)$  if a bulk supercell is used as marker. The latter approach is used in this work.

Defect migration and transformation paths were investigated with the help of a climbing image nudged elastic band (CI-NEB) method.<sup>38,39</sup> The procedure starts with an initial guess of an array of intermediate structures between initial and starting atom coordinates. These were mostly obtained from linear interpolation between both end configurations. Each pair of consecutive structures is then coupled by a virtual elastic band. While the elastic band introduces a penalty for too small or too large distances between neighboring structures, it also brings them into contact with the minimum energy path (MEP) connecting initial and final states. After performing an iterative series of atomic relaxation steps subject to the elastic band constraints (standard NEB method), the highest energy structure (*climbing image*) within the array is identified. Then, this image moves up the potential energy surface along the elastic band and down the potential surface perpendicular to the band.<sup>38</sup> This method has been successfully used to study defect diffusion and reorientation mechanisms in Si and Ge.<sup>40,41</sup>

## IV. EXPERIMENTAL RESULTS

### A. $V_3$ -related transformations upon annealing of electron-irradiated Si diodes in the temperature range 300–380 K

As previously mentioned in the introduction, in our previous studies (Refs. 15 and 37) the  $E4/E5$  DLTS signals, which are frequently observed in the spectra of  $n$ -type silicon irradiated with high energy particles,<sup>11,19,42–44</sup> were assigned to the second and first acceptor levels of the silicon trivacancy in the PHR configuration. In the DLTS spectra of electron-irradiated  $p$ -type Si the signals related to the traps having activation energies for hole emission to the valence band of 0.193 eV ( $H_{193}$ ) and 0.106 eV ( $H_{106}$ ) were associated with the first and second donor levels of the  $V_3$  defect in the PHR configuration.<sup>16</sup> It was found that the  $E4/E5$  and  $H_{193}/H_{106}$  signal pairs disappeared after storage for a few weeks of the irradiated Si samples at room temperature or after shorter anneals in the temperature range 50–100 °C. The disappearance of the  $V_3$ [PHR]-related signals resulted in the growth of DLTS signal due to an electron trap with the activation energy for electron emission to the conduction band of 0.075 eV ( $E_{75}$ ).<sup>15,16</sup> The  $E_{75}$  trap was assigned to the first acceptor level of the silicon trivacancy in the FFC configuration.<sup>15</sup> In this part of the paper the results of our study of the  $V_3$ [PHR]  $\rightarrow$   $V_3$ [FFC] transformations monitored as changes in concentrations of the traps giving rise to the  $E4/E5$ ,  $E_{75}$ , and  $H_{193}/H_{106}$  DLTS signals are reported. A question of particular interest was if the transformation rate depends on the charge states of  $V_3$  in the initial PHR configuration.



It should be noted first that some results on the disappearance of the  $E4/E5$  DLTS signals in irradiated  $n$ -type Si samples upon their annealing in the temperature range 25–90 °C were reported in Refs. 11 and 44. In both works the process was found to be described satisfactorily by first-order reaction kinetics. In Ref. 11 it was found that the disappearance rates did not depend on the oxygen content and for the samples with phosphorus concentration in the range  $(1-2) \times 10^{12} \text{ cm}^{-3}$  the activation energy of the process was found to be  $1.13 \pm 0.1 \text{ eV}$ . This value was derived from an analysis of the annealing data in the temperature range 35–90 °C. The Fermi level in those samples upon annealing was in the range 0.44–0.53 eV below the conduction band edge, so the majority of the  $V_3[\text{PHR}]$  centers were in the neutral charge state. In Ref. 44 the activation energy of the  $E4$  signal elimination in the temperature range 23–65 °C was determined as 1.27 eV in the samples with doping level of about  $5 \times 10^{12} \text{ cm}^{-3}$ . The Fermi level in those samples upon annealing was in the range 0.39–0.50 eV below the conduction band edge. The first acceptor level of the  $V_3[\text{PHR}]$  defect is just in the middle of this range  $V_3[\text{PHR}](-/0) = E_c - 0.46 \text{ eV}$ ,<sup>15</sup> so at lower annealing temperatures the  $V_3[\text{PHR}]$  centers were mainly in the singly negatively charged state, while at higher annealing temperatures the majority of the centers were in the neutral charge state.

We have studied the kinetics of disappearance of the  $E4$  signal and formation of the  $E_{75}$  signal in two electron-irradiated  $p^+-n-n^+$  diodes on the same chip upon their isothermal annealing at six temperature points in the range 310–360 K. One of the diodes was annealed under reverse bias, while no bias was applied to another diode upon annealing. In the diode, which was annealed with zero bias, the Fermi level varied from  $E_c - 0.34 \text{ eV}$  to  $E_c - 0.40 \text{ eV}$  in the above temperature range, so, the  $V_3[\text{PHR}]$  defects were predominantly in the singly negatively charged state upon annealing. In the depletion region of the diode which was annealed with the reverse bias applied, the Fermi level was in the middle of the gap, thus the  $V_3[\text{PHR}]$  centers were in the neutral charge state. Figure 2 shows the concentration change kinetics of the  $V_3$  defect in the PHR and FFC configurations upon isothermal annealing at 330 K in the diode, which was annealed with the reverse bias applied. It appears that both the decay of the  $V_3$  defect in the PHR configuration and the growth of the  $V_3[\text{FFC}]$  concentration can be described by monoexponential functions with matching decay and growth rates. Similar  $V_3[\text{PHR}] \rightarrow V_3[\text{FFC}]$  transformations were observed in the diode, which was annealed at 330 K with zero bias, however, the decay and growth rates in this diode differ from those obtained for the diode, which was annealed with the bias.

Figure 3 shows Arrhenius plots of the  $V_3[\text{PHR}] \rightarrow V_3[\text{FFC}]$  transformation rates obtained from an analysis of kinetics of the process upon isothermal annealing of the reverse-biased and zero-biased  $p^+-n-n^+$  diodes. In the case of annealing with the applied reverse bias, the activation energy ( $\Delta E_T$ ) and pre-exponential factor ( $A_0$ ) for the  $V_3[\text{PHR}] \rightarrow V_3[\text{FFC}]$  transformation have been found to be  $1.16 \pm 0.02 \text{ eV}$  and  $2.75 \times 10^{13} \text{ s}^{-1}$ , while for the annealing without bias the  $\Delta E_T$  and  $A_0$  values have been determined as  $1.22 \pm 0.02 \text{ eV}$  and  $1.6 \times 10^{14} \text{ s}^{-1}$ . Some preliminary conclusions about the transformation process can be drawn from an analysis of the above values. First, the  $A_0$  values obtained are close

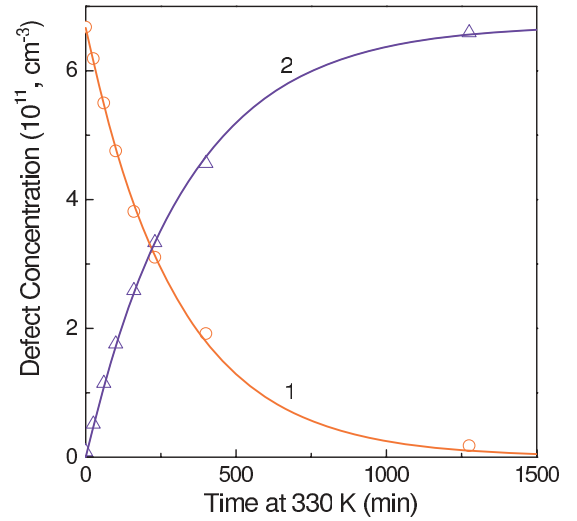


FIG. 2. (Color online) Changes in concentrations of the  $V_3$  defect in the (1) PHR and (2) FFC configurations in an electron-irradiated  $p^+-n$  diode upon isothermal annealing at 330 K with applied reverse bias of  $-12 \text{ V}$ . The reverse bias upon Laplace-DLTS measurements, from which the concentrations were derived, was  $-10 \text{ V}$ . Solid lines are calculated with the use of monoexponential decay and growth functions with parameters adjusted for the best fits to the experimental data.

and characteristic for the process of atomic reconstruction. Furthermore, it appears that the  $V_3[\text{PHR}] \rightarrow V_3[\text{FFC}]$  transformation occurs with similar rates for both neutral and singly negatively charged  $V_3[\text{PHR}]$  defects, and that the respective activation energies are very close. If the transformation could involve different defect reactions in the different charge states or occur predominantly in one of the charge states, the activation energies and  $A_0$  values of the process would differ significantly.<sup>45</sup> The differences between the activation energies and  $A_0$  values determined is not large. This observation

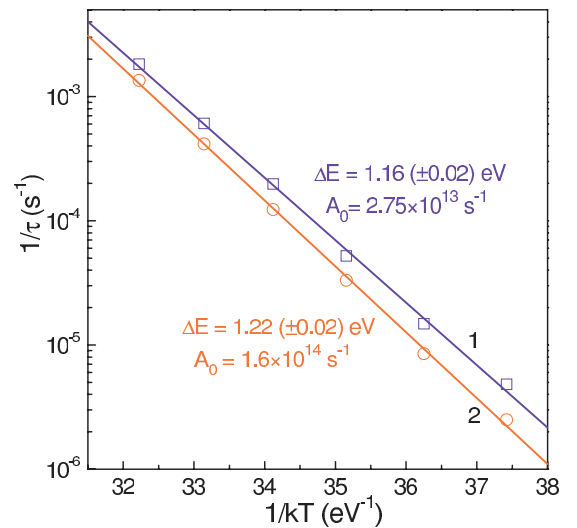


FIG. 3. (Color online) Arrhenius plots of the  $V_3[\text{PHR}] \rightarrow V_3[\text{FFC}]$  transformation rates in electron-irradiated  $n$ -type epi-Si diodes, which were annealed isothermally with (1) reverse bias of  $-12 \text{ V}$  and (2) no bias.

indicates a similar transformation path for both the charge states of  $V_3$ [PHR]. At the final state of the transformation, the  $V_3$  defect is in the neutral FFC configuration at all the annealing temperatures. So, the obtained activation energy of the process, which starts from the singly negatively charged  $V_3$ [PHR<sup>-</sup>] defect includes the depth of the  $V_3$ [FFC](-/0) occupancy level with respect to the conduction band, that is assumed to be approximately 0.075 eV if we neglect entropy effects. Thus, the energy barrier for the  $V_3$ [PHR<sup>-</sup>]  $\rightarrow$   $V_3$ [FFC<sup>-</sup>] transformation in the singly negatively charge state should be about  $1.22 - 0.075 = 1.145$  eV. This value is very close to the activation energy obtained for the  $V_3$  transformation in the neutral charge state, 1.16 eV.

The reaction rates for the  $V_3$ [PHR]  $\rightarrow$   $V_3$ [FFC] transformation upon isothermal annealing of the  $n^+-p-p^+$  diodes in the temperature range 300–370 K have been found to be very close for both the reverse-biased and zero-biased annealed diodes and the values derived are close to those for the  $p^+-n-n^+$  diodes annealed with the reverse bias applied. We can understand these results if (a) the process consists of just the  $V_3$  defect transformation and so is impurity independent and (b) in the  $p$ -based diodes the  $V_3$  defects were in the neutral PHR configuration at the beginning of the  $V_3$ [PHR<sup>0</sup>]  $\rightarrow$   $V_3$ [FFC<sup>0</sup>] transformation at all the annealing temperatures and applied biases. The Fermi level in the zero-biased  $n^+-p-p^+$  diodes varied from  $E_v + 0.23$  eV to  $E_v + 0.38$  eV in the chosen annealing temperature range, so it was always above the first donor level of the  $V_3$  defect in the PHR configuration, which is at  $E_v + 0.19$  eV.<sup>16</sup>

### B. $V_2$ and $V_3$ DLTS changes in oxygen-containing $e$ -irradiated Si samples upon annealing in the temperature range 200–300 °C

Figure 4 shows the changes in concentrations of the  $V_2$  and  $V_3$  (both in the PHR and FFC configurations) defects in an electron-irradiated epi-Si  $p^+-n$  diode and in an

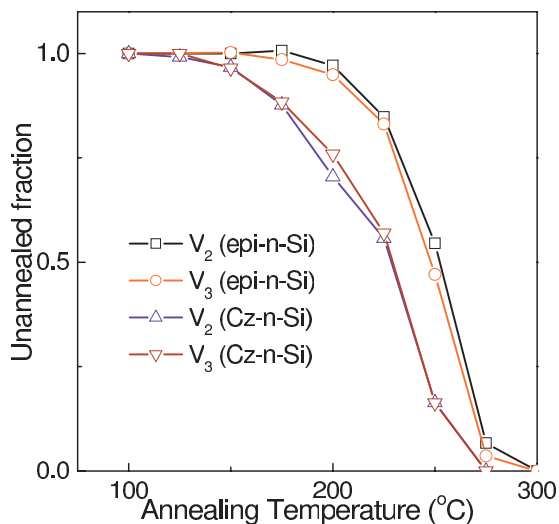


FIG. 4. (Color online) Changes in unannealed fractions of the  $V_2$  and  $V_3$  defects in an electron-irradiated epi-Si  $p^+-n$  diode and in an electron-irradiated Cz-Si sample with a Schottky barrier diode upon their 30-min isochronal annealing.

electron-irradiated Cz-Si sample with a Schottky barrier diode upon their 30-min isochronal annealing. The annealing behaviors of the  $V_2$  and  $V_3$  centers are very similar in either the epi-Si or Cz-Si samples but there is a significant difference between those for different materials. There is strong experimental evidence that the elimination of divacancies in oxygen-rich Si samples is associated with their interaction with oxygen atoms and results in the formation of a  $V_2O$  defect.<sup>21,46</sup> An analysis of changes in conventional DLTS and Laplace DLTS spectra upon isochronal annealing has shown that the transformation of energy levels due to the  $V_2$  defect to those assigned previously to  $V_2O$  occurs in both the electron-irradiated epi- $n$ -Si and Cz- $n$ -Si samples studied in the present work. So, the difference in the annealing temperature range of the  $V_2$  defect in the epi- $n$ -Si and Cz- $n$ -Si samples can be easily explained by the difference in the oxygen concentration in the corresponding materials. Taking into account similar structures and electronic properties of the  $V_2$  and  $V_3$ [PHR] defects, it is tempting to suggest that the disappearance of  $V_3$  upon isochronal annealing, similar to that of divacancies, is associated with the diffusion of trivacancies in the (110) planar configuration and their interaction with interstitial oxygen atoms.<sup>15–17</sup> However, one should mind that for the Fermi level position in the temperature range 200–300 °C where the  $V_2$  and  $V_3$  defects disappear, the energetically favorable configuration of  $V_3$  is the FFC one. Electronic properties of  $V_3$  in this configuration differ significantly from those of the  $V_3$  and  $V_2$  defects in the (110) planar configurations, so, the migration mechanism of  $V_3$  upon annealing at  $T > 200$  °C could be quite different from that of  $V_2$  (details of the  $V_2$  migration mechanism were given in Ref. 47) and similar annealing behaviors of the  $V_2$  and  $V_3$  defects could be just a coincidence.

To obtain further details on the annealing mechanisms of the  $V_2$  and  $V_3$  defects we have carried out isothermal annealing of the irradiated epi- $n$ -Si diodes in the temperature range 230–270 °C. The Fermi level in this temperature range in the samples studied is close to the middle of the gap, so, both the centers are primarily in their neutral charge states during annealing. It has been found that the kinetics of the decay of both the  $V_2$  and  $V_3$  defects upon isothermal annealing in the above temperature range are described well by monoexponential functions with close rate constants. Figure 5 shows the decay kinetics of the  $V_2$  and  $V_3$  upon annealing at 270 °C. The kinetics of the anticorrelated formation of the  $V_2O$  and  $V_3O$  defects are also found to be similar (Fig. 5). It should be mentioned here that the decay kinetics of  $V_2$  and  $V_3$  and the appearance kinetics of the  $V_2O$  and  $V_3O$  centers have been compared in the same diode.

Figure 6 shows Arrhenius plots of the elimination rate constants for the  $V_2$  and  $V_3$  defects in the electron-irradiated  $n$ -type epi-Si and Cz-Si samples. The activation energy and pre-exponential factor of the process for  $V_2$  have been found to be  $1.41 \pm 0.05$  eV and  $9.2 \times 10^9$  s<sup>-1</sup>, while the values for  $V_3$  have been determined as  $1.47 \pm 0.04$  eV and  $3.8 \times 10^{10}$  s<sup>-1</sup>. Evidence for the involvement of oxygen in the elimination reaction of  $V_3$  has been obtained from a comparison of the reaction rates in epi-Si and Cz-Si diodes. The reaction rate is found to be about three times faster in Cz-Si diodes, where  $[O_i]$  was  $1.0 \times 10^{18}$  cm<sup>-3</sup>, compared to those in epi-Si diodes ( $[O_i] \approx 3.5 \times 10^{17}$  cm<sup>-3</sup>).

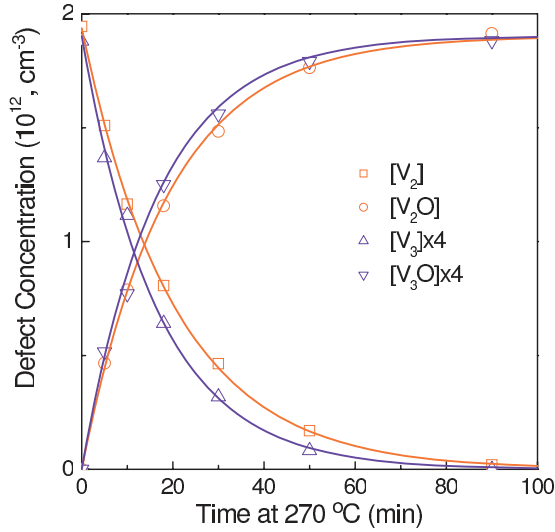


FIG. 5. (Color online) Changes in concentrations of the  $V_2$ ,  $V_3$ ,  $V_2O$ , and  $V_3O$  defects in an electron-irradiated epi-Si  $p^+-n$  diode upon isothermal annealing at 270 °C. Concentrations of the  $V_3$ -related defects are multiplied by 4. Solid lines are calculated with the use of monoexponential decay and growth functions with parameters adjusted for the best fits to the experimental data.

## V. THEORETICAL RESULTS

### A. Atomic models and electronic structure of $V_3$

In broad terms, our structural calculations of  $V_3$  in Si confirm previous density-functional studies.<sup>14,15</sup> The trivacancy has two particularly stable forms, namely a PHR form with  $C_{2v}$  (orthorhombic) symmetry shown in Fig. 1(a) made of three neighboring vacant sites, and a FFC form with  $D_3$  (trigonal) symmetry shown in Fig. 1(d) made of three Si atoms edging six vacant sites of a hexavacancy ring. Two new metastable structures whose relevance will become clear in the following are also depicted in Figs. 1(b) and 1(c).

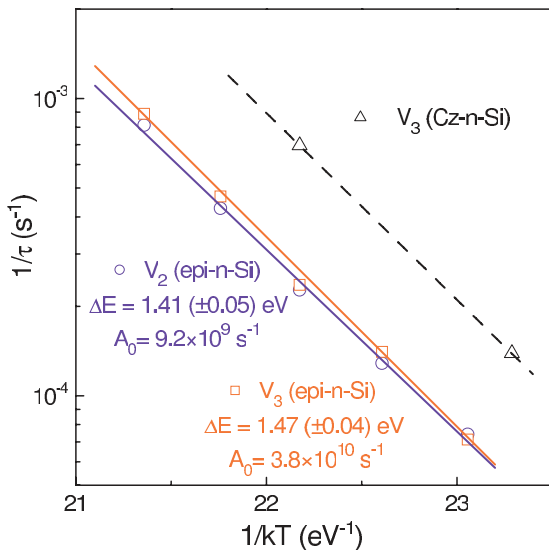


FIG. 6. (Color online) Arrhenius plots of the elimination rate constants for the divacancy and trivacancy in electron-irradiated  $n$ -type epi-Si and Cz-Si samples.

TABLE I. Relative energies (in eV) of fully relaxed trivacancy structures in charge states from doubly positive to doubly negative. Neutral spin-0 ( $S = 0$ ) and spin-1 ( $S = 1$ ) states are also reported. All energies are relative to the ground-state configuration with the same charge. Table cells with  $C_1$  or  $C_2$  labels refer to unstable structures, indicating the structure attained after atomic relaxation.

State	$D_3$ (FFC)	$C_2$	$C_1$	$C_{2v}$ (PHR)
++	0.17	0.46	$C_2$	0.00
+	0.03	$C_1$	0.64	0.00
0, $S = 0$	0.00	$C_1$	0.86	0.26
0, $S = 1$	1.13	0.98	$C_2$	0.34
-	0.02	0.72	$C_2$	0.00
=	0.36	0.70	$C_2$	0.00

From the relative energies of geometrically relaxed structures (see Table I) we found that among neutrally charged diamagnetic structures,  $V_3[\text{FFC}]$  is the ground state whereas  $V_3[\text{PHR}]$  is metastable by 0.26 eV. Unlike in Ref. 15, we found that the spin-1 state  $V_3[\text{PHR}^{0,S=1}]$  is less favored than the spin-0 one, and that lies 0.34 eV above the ground state. This small discrepancy may arise from a propensity of the local exchange treatment to favor high-spin states that could be overlocalized when the host is confined to a cluster.<sup>15</sup> Conversely, for charged supercells the most stable form was the  $V_3[\text{PHR}]$  structure. The  $V_3[\text{FFC}]$  form was found metastable by 0.17 eV, 0.03 eV, 0.02 eV, and 0.36 eV for the ++, +, - and = charge states, respectively, and these figures also compare well with previous results.<sup>15</sup> Structures  $V_3[C_2]$  and  $V_3[C_1]$  are rather similar. They are formed when two of the three numbered Si atoms in Fig. 1, say the  $\text{Si}_1$ - $\text{Si}_2$  dimer, occupy regular crystalline sites. These form a pair of unsaturated electron radicals represented by solid sticks (red sticks in the online edition) in Figs. 1(b) and 1(c). Four other radicals forming two pairs of elongated reconstructions,  $\text{Si}_4$ - $\text{Si}_4'$  and  $\text{Si}_5$ - $\text{Si}_5'$ , are depicted as “banana” bonds in the same figures. The relative energies of  $V_3[C_2]$  and  $V_3[C_1]$  defects are estimated to differ by less than  $\sim 0.2$  eV, and they lie between 0.5 and 1 eV above the most stable structure (see Table I), depending on their charge state. The symmetric dimer structure with  $C_2$  symmetry is lower in energy, except for the positive and neutral  $S = 0$  (diamagnetic) states, where it relaxes to the buckled (asymmetric)  $V_3[C_1]$  defect. The structure where only one of the numbered Si atoms was located at a substitutional vacant site [the other two being positioned as in Fig. 1(d)] was unstable and returned to  $V_3[\text{FFC}]$  upon atomic relaxation, irrespective of its charge state.

Let us now look more closely at the geometry and electronic structure of these defects. Unless specified, the following analysis refers to neutral diamagnetic states only. The  $V_3[\text{PHR}]$  form, comprises three neighboring Si vacancies that define its main (110) lying plane [see Fig. 1(a)]. The electronic band structure of this defect is shown in Fig. 7(a), where defect bands within the gap can be separated into two pairs. States of the low-energy pair of bands are symmetric with respect to the (110) mirror plane and arise from two equivalent dangling bonds ( $db$  and  $db'$ ) depicted as solid sticks (red sticks in the online edition) in Fig. 1(a). These radicals are separated by 7.312 Å and produce weakly coupled symmetric

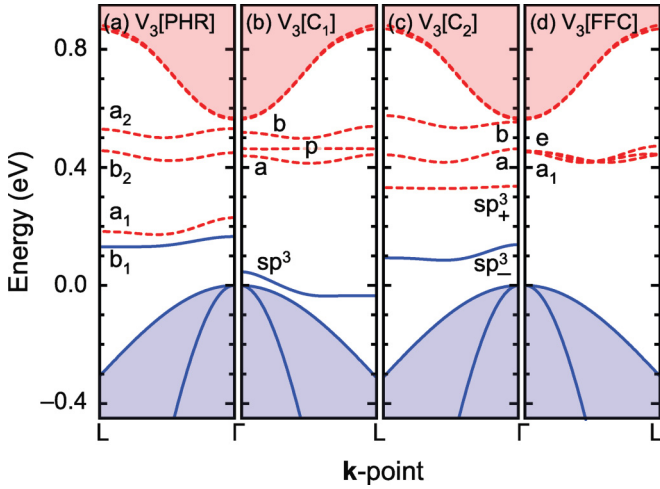


FIG. 7. (Color online) One-electron band structure from spin-averaged Kohn-Sham levels of neutral  $V_3$  defects (in 512 atom supercells) along the  $[111]$  direction in reciprocal space. Occupied and empty bands are shown in solid (blue) and dashed (red) lines, respectively. Only the topmost valence band and lowest conduction band states from bulk are shown (limiting shadowed areas).  $D_3$  and  $C_{2v}$  symmetry representation of gap levels at  $\mathbf{k} = \Gamma$  is shown for gap states of  $V_3[\text{FFC}]$  and  $V_3[\text{PHR}]$ , respectively. For  $V_3[\text{C}_2]$  and  $V_3[\text{C}_1]$  structures we adopt an *ad hoc* band labeling scheme (see text).

$\psi_{a_1} = 1/\sqrt{2}|db + db'\rangle$  and antisymmetric  $\psi_{b_1} = 1/\sqrt{2}|db - db'\rangle$  orbitals. The lowest energy  $\psi_{b_1}$  state is fully occupied and is shown in Fig. 8(a). States  $\psi_{b_1}$  and  $\psi_{a_1}$  are responsible for the deep donor and acceptor activity of  $V_3[\text{PHR}]$ . States from the high-energy pair,  $\psi_{b_2}$  and  $\psi_{a_2}$ , are symmetric with respect to the  $(1\bar{1}0)$  plane and result from the coupling of six off-plane Si dangling bonds [ $j$  and  $j'$  atoms in Fig. 1(a) with  $j = 1, 3, 5$ ].

In  $V_3[\text{FFC}]$ , the three core  $\text{Si}_i$  atoms (with  $i = 1, \dots, 3$ ) are each able to passivate four radicals in the hexavacancy. However, inspecting their bonding geometry, we realize that a considerable departure from  $T_d$  symmetry takes place. Their  $\text{Si}_i\text{-Si}_b$  and  $\text{Si}_i\text{-Si}_c$  bonds (approximately perpendicular to the  $[111]$  symmetry axis) are 2.435-Å long, whereas the two other bonds  $\text{Si}_i\text{-Si}_a$  and  $\text{Si}_i\text{-Si}_{a'}$  (nearly parallel to the  $[111]$  symmetry axis) are 2.593 Å. These are particularly long if compared to the bulk Si-Si first neighbor distance of 2.335 Å. Angles formed by the  $\text{Si}_a\text{-Si}_i\text{-Si}_{a'}$  and  $\text{Si}_b\text{-Si}_i\text{-Si}_c$  structures are  $160^\circ$  and  $108^\circ$ , whereas the other four  $\text{Si}_{a/a'}\text{-Si}_i\text{-Si}_{b/c}$  angles are  $90^\circ$  or  $103^\circ$ . The long and flat  $\text{Si}_a\text{-Si}_i\text{-Si}_{a'}$  trimer units have their bond lengths and angles particularly deformed. Each of these units is responsible for an empty antibonding state  $|i\rangle$  (with  $i = 1, \dots, 3$ ), just below the conduction band bottom. A trigonal arrangement of degenerate  $|1\rangle$ ,  $|2\rangle$ , and  $|3\rangle$  states in a cubic lattice results in hybrid singlet  $\psi_{a_1} = 1/\sqrt{3}|i + j + k\rangle$  and doublet  $\psi_e = \alpha\psi_{e,\alpha} + \beta\psi_{e,\beta}$  states, with  $\psi_{e,\alpha} = 1/\sqrt{6}|i + j - 2k\rangle$  and  $\psi_{e,\beta} = 1/\sqrt{2}|i - j\rangle$ , and  $\alpha$  and  $\beta$  being normalizing coefficients such that  $\alpha^2 + \beta^2 = 1$ . Inspection of the Kohn-Sham band structure shown in Fig. 7(d) allows us to follow these states in reciprocal space. The figure shows three high lying empty bands within the gap ( $a_1 + e$ ). We note that the singlet and the doublet show a dispersion below 0.1 eV and their minute coupling energy separation results from the large distance (4.121 Å) between the  $\text{Si}_i$  atoms.

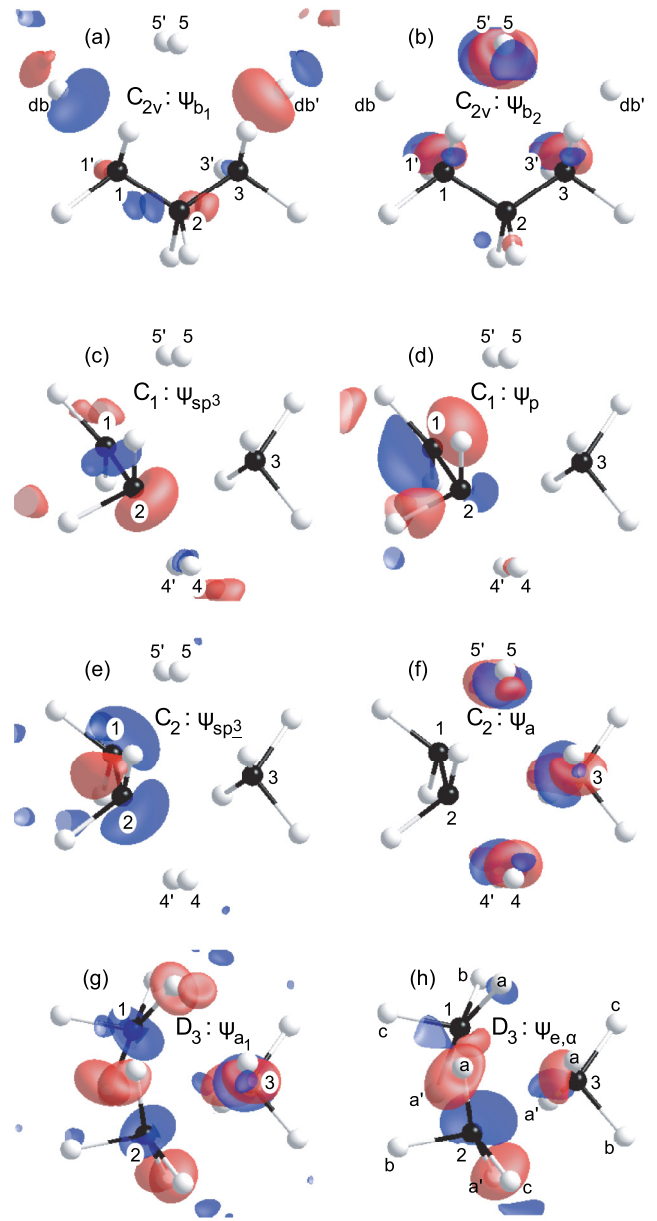


FIG. 8. (Color online) Kohn-Sham state iso-surfaces,  $\psi_{\lambda,\mathbf{k}}(\mathbf{r})$  at  $\mathbf{k} = \Gamma$  and selected levels  $\lambda$ , for  $V_3$  in Si. In (a), (c), and (e) we find  $\lambda = \text{HOKO}$  states for  $V_3[\text{PHR}]$ ,  $V_3[\text{C}_2]$ , and  $V_3[\text{C}_1]$ , respectively, whereas (b), (d), and (f) show  $\lambda = \text{LUKO}$  states for the same structures. States in (g) and (h) correspond to  $\lambda = a_1$  and  $\lambda = e(\alpha)$  states for  $V_3[\text{FFC}]$ , respectively. HOKS and LUKS stand for highest occupied Kohn-Sham state and lowest unoccupied Kohn-Sham state, respectively. Iso-surface values are  $\psi = 0.06$  and  $\psi = -0.06$  (respectively, colored in red and blue in the online edition). Structure orientation, atom coloring scheme, and labeling are consistent with Fig. 1.

At  $\mathbf{k} = \Gamma$  the  $a_1$  level lies only 0.03 meV below the doublet and they are depicted in Figs. 8(g) and 8(h) ( $\alpha$  component), respectively. As reported below, the  $\psi_{a_1}$  state is able to trap an electron, being responsible for an acceptor level.

The  $V_3[\text{C}_2]$  structure has two equivalent threefold-coordinated  $\text{Si}_1$  and  $\text{Si}_2$  atoms that make a 2.266-Å strong bond. These produce  $sp^3$ -like dangling bonds [represented



by solid sticks in Fig. 1(c)], that couple into solid  $\psi_{sp^3}$  and empty  $\psi_{sp^3}$  states as shown in the lower half of the gap in Fig. 7(c). The wave-function iso-surface for the highest occupied  $sp^3$  state is shown in Fig. 8(e). It strongly resembles the symmetric Si(001)-(2 × 1) reconstructed surface dimer states, where dangling bonds almost perpendicular to the surface, pair into  $\pi$ - and  $\pi^*$ -like states.<sup>48</sup> Also like the surface, this structure is unstable against charge transfer between dangling bonds with the consequent distortion of the dimers (buckling).<sup>49</sup> Accordingly, we found that the  $V_3[C_1]$  structure with a 2.276-Å Si<sub>1</sub>-Si<sub>2</sub> bond length, is more stable than the symmetric dimer in the positive and diamagnetic neutral charge states (see Table I). As depicted in Figs. 8(c) and 8(d), it leads then to occupied states localized on  $sp^3$ - and  $p$ -like dangling bonds on atoms Si<sub>2</sub> and Si<sub>1</sub>, respectively. The symmetric  $C_2$  structure is clearly more stable than  $C_1$  in the ++, neutral spin-1, and double minus charge states. In the minus charge state,  $V_3[C_2]$  was marginally more stable than  $V_3[C_1]$ .

### B. Electrical levels of $V_3$

Now we turn to the electrical properties of  $V_3$  in silicon. These results are based on ionization energies of defective supercells compared to the same calculation for bulk. In Sec. III the marker method was introduced, and an acceptor level for  $V_3$ [FFC] was obtained at  $E_c - 0.16$  eV. The acceptor level is close to the experimental  $E_{75}$  electron trap at  $E_c - 0.075$  eV, and it is represented by the  $(-/0)$  level on the left-hand side of Fig. 9(a). A donor level is also calculated to lie very close to the valence band top. However, from the band structure in Fig. 7(a) we could not identify a defect-related occupied band edging the valence band top, and hence we assume that  $V_3$ [FFC] is not a donor. Calculation of second ionizations  $I(+/-++)$  and

$I(=/-)$  also led to unstable double donor and double acceptor levels outside the gap for  $V_3$ [FFC].

Although the FFC form is the most stable structure in the neutral charge state, the PHR structure was found more stable in the ++, +, -, and = states by 0.17, 0.03, 0.02, and 0.36 eV, respectively. For the ionization energies of  $V_3$ [PHR] we obtain  $I_d$  values of 5.16, 5.29, 5.90, and 6.04 eV for  $(+/++)$ ,  $(0/+)$ ,  $(-/0)$ , and  $(=/-)$  transitions, respectively. This places first and second donor levels at  $E_v + 0.29$  eV and  $E_v + 0.15$  eV, as well as first and second acceptor levels at  $E_c - 0.43$  eV and  $E_c - 0.31$  eV, respectively, in very good agreement with respective DLTS levels measured at  $E_v + 0.193$  eV and  $E_v + 0.116$  eV for first and second donor states, and at  $E_c - 0.458$  eV and  $E_c - 0.359$  eV for first and second acceptor states. These calculations are represented by the solid lines on the right-hand side of Fig. 9(a). The donor levels arise from ionization of the doubly occupied  $\psi_{b_1}$  state, whereas the acceptor levels result from trapping up to two electrons at the  $\psi_{a_1}$  empty state (see Sec. V A).

From Eqs. (4)–(6) we produced the diagram in Fig. 9(b) showing the formation energy of  $V_3$  as a function of the electron chemical potential. This works like a *defect phase diagram* and is particularly instructive if we wish to picture out occupancy states of bistable centers under thermodynamic equilibrium conditions. By solving  $E_f[\text{FFC}^0] = E_f[\text{PHR}^{++}]$  and  $E_f[\text{FFC}^0] = E_f[\text{PHR}^-]$  we found  $V_3(0/++)$  and  $V_3(= / 0)$  levels at  $E_v + 0.11$  eV and  $E_c - 0.27$  eV, respectively, thus showing a negative- $U$  ordering on both donor and acceptor states. It also indicates that despite  $V_3$ [PHR] having deep donor and acceptor levels, in equilibrium the defect will be in the neutral FFC state for a wide range of Fermi energies ( $E_v + 0.11$  eV  $\leq E_f \leq E_c - 0.27$  eV). Formation energies of neutral FFC and PHR trivacancies are 6.53 and 6.79 eV. These figures compare fairly well with  $E_f$  values of 6.20 and 6.80 eV, respectively, that were reported in Ref. 14.

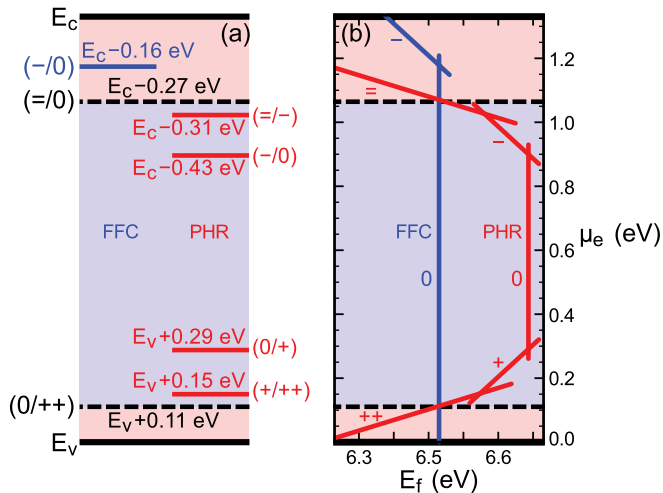


FIG. 9. (Color online) Calculated electrical level diagram (a) and formation energy ( $E_f$ ) diagram as a function of the electron chemical potential ( $\mu_e$ ) (b) for  $V_3$  in silicon. The electrical level diagram in (a) shows  $V_3$ [FFC] levels (left),  $V_3$ [PHR] levels (right), and  $V_3$  occupancy levels (dashed lines). Formation energies were obtained from Eqs. (4)–(6) and they are labeled with their respective structures and charge states.

### C. Transformation and migration mechanisms

Defect and atomic motion in solids is usually limited by the kinetics of breaking and formation of bonds. In pointlike vacancy defects, host atoms move in opposite direction to vacant sites, where radicals, and reconstructed and twisted bonds play a major role because of their reactivity and promptness for structural change. However, for extended defects such as  $V_3$ [FFC], diffusion or transformation mechanisms usually involve collective atomic motion, and the search for such paths requires sampling of large portions of the configurational space, for instance, by means of computationally intensive molecular dynamics calculations. This approach, combined with a first-principles Hamiltonian, is intractable when a large volume of the host material is needed to adequately account for strain fields and other long-range effects.<sup>50,51</sup> Our strategy was then to hypothesize transformation and migration mechanisms, hoping to find activation barriers compatible with the annealing kinetics measurements. Several transformation paths were investigated by setting specific end structures and intermediate configurations to be relaxed by the CI-NEB method. For practical reasons, we restrict our analysis to four transformation coordinates,  $Q_k$  with  $k = 1, \dots, 4$ , from which we can envisage possible transformation and migration

mechanisms for the trivacancy. Accordingly,  $Q_1$ ,  $Q_2$ ,  $Q_3$ , and  $Q_4$  refer to  $V_3[\text{PHR}] \rightleftharpoons V_3[C_{2h}]$ ,  $V_3[\text{PHR}] \rightleftharpoons V_3[C_1]$ ,  $V_3[C_1] \rightleftharpoons V_3[C_2]$ , and  $V_3[C_2] \rightleftharpoons V_3[\text{FFC}]$  transformations, respectively. The structure with  $C_{2h}$  symmetry will be introduced below. During the transformations, the electronic charge density adapts instantaneously to atomic motion (adiabatic approximation), and we neglect any change of charge or spin state along each step. For example, for a charge state  $q$  and general coordinate  $Q_1$ , we have forward  $\Delta E_T^q[\text{PHR} \rightarrow C_{2h}]$  and reverse  $\Delta E_T^q[\text{PHR} \leftarrow C_{2h}]$  transformation barriers, which differ by the relative energy of the respective end structures.

Let us first assume that the Fermi level is near midgap and most  $V_3$  complexes are in the neutral charge state. Although  $V_3^0[\text{FFC}]$  is *a priori* the initial/final state of the migration mechanism, we note that the measurements indicate that E4 and E5 DLTS bands (assigned to  $V_3[\text{PHR}]$ ) are readily formed upon room-temperature irradiation. Hence, a sufficiently high  $V_3^0[\text{PHR}] \rightarrow V_3^0[\text{FFC}]$  transformation barrier (higher than the migration barrier) could allow the planar  $V_3$  to migrate while preventing the structure to attain the FFC ground state. We start by investigating this premise, and like the divacancy in Si,<sup>47</sup>  $V_3[\text{PHR}]$  is firstly proposed to migrate with end atoms moving across the vacant space as shown in Fig. 10(a). This mechanism is represented by the general coordinate  $Q_1$ . After relaxation of seven intermediate structures connected by an elastic band, we found that the saddle point is the structure with  $C_{2h}$  symmetry shown in Fig. 10(b), where the displaced Si atom lies at the bond-center site, and midway to the furthest vacant site. The respective  $V_3[\text{PHR}] \rightarrow V_3[C_{2h}]$

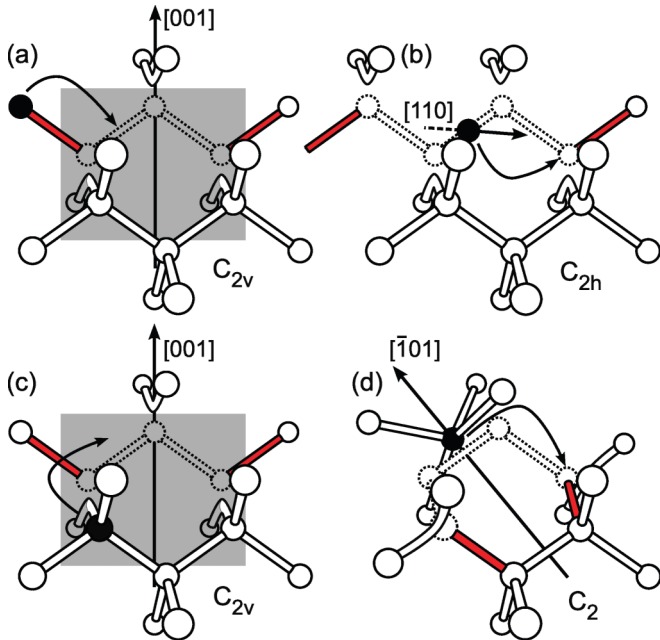


FIG. 10. (Color online) Two migration mechanism candidates for  $V_3$ . Subfigures (a) and (c) depict initial ground-state structures for each mechanism along with their respective first steps (represented by curved arrows suggesting atomic motion) towards saddle point structures shown in (b) and (d). Subfigures (b) and (d) also suggest the atomic motion towards the final displaced ground-state forms (curved arrows). Structure orientation, and atom and bond coloring schemes are identical to those adopted in Fig. 1.

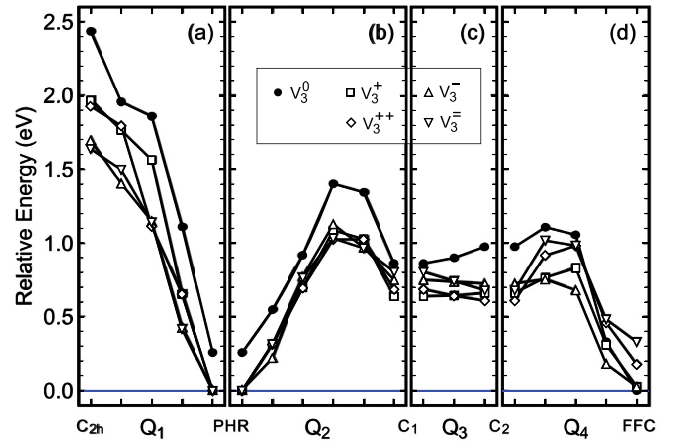


FIG. 11. (Color online) Minimum energy paths obtained from CI-NEB calculations between the most relevant  $V_3$  structures and charge states for this work. Relative energies of neutral and charged defects were calculated with respect to FFC and PHR structures, respectively. Lines that connect calculated data are uniquely shown for eye guidance purposes.

MEP is shown in Fig. 11(a) by the line connecting solid circles. This corresponds to half of the whole migration mechanism, with the remaining path being equivalent by symmetry. The mechanism has a barrier of  $\Delta E_M^0 = 2.18$  eV, which is too high to account for the experimental observations and should be ruled out. The coordinate  $Q_1$  accounts solely for the migration along a unique (110) symmetry plane as depicted in Figs. 10(a) and 10(b). A migration mechanism that accounts for the reorientation of the defect would have to involve the displacement of an off-plane Si atom as suggested in Figs. 10(c) and 10(d). The calculated barrier for such a  $V_3[\text{PHR}] \rightarrow V_3[C_2]$  step was 2.05 eV, which is also too high to account for the measurements.

An alternative  $V_3[\text{PHR}] \rightarrow V_3[C_2]$  migration mechanism involves a three-atom correlated motion of  $\text{Si}_1$ ,  $\text{Si}_2$ , and  $\text{Si}_3$  as depicted in Figs. 1(a)–1(c). These illustrate the end structures of the two-step ( $Q_2, Q_3$ ) transformation path. The MEP for neutral  $V_3$  along ( $Q_2, Q_3$ ) is represented in Figs. 11(b) and 11(c) by the solid circles. Along  $Q_2$  forward direction, each PHR configuration can be transformed into four equivalent  $C_1$  configurations, and each of these may be transformed into a single  $C_2$  defect along  $Q_3$ . Up to this point we arrive at the halfway point of the migration step. Along the reverse transformation path, each  $C_2$  defect can evolve into two equivalent  $C_1$  structures, each of which can be transformed to a single PHR configuration. However, one of these  $C_2 \rightarrow C_1 \rightarrow \text{PHR}$  steps will lead to the initial  $C_{2v}$  form, so that overall, a total of four symmetry equivalent final configurations (lying on different hexagonal rings) can be attained from each initial structure. The saddle point configuration was found to lie between PHR and  $C_1$  configurations, and that corresponds to  $\Delta E_T[\text{PHR}^0 \rightarrow C_1^0] = 1.15$  eV. Although this is now closer to the measured diffusion barrier, inspection of Fig. 11(d) clearly shows that once the  $\text{PHR} \rightarrow C_1$  transformation barrier is overcome, the small barriers along  $Q_3$  and  $Q_4$  may also be surmounted and  $V_3[\text{FFC}]$  may be readily attained. Hence, a metastable migration mechanism for neutral  $V_3$  in the

planar form based on the premise of a high barrier separating  $V_3[\text{FFC}^0]$  from  $V_3[\text{PHR}^0]$  should be discarded as well. In fact the calculated overall barrier  $\Delta E_T[\text{PHR}^0 \rightarrow \text{FFC}^0] = 1.15$  eV accounts rather well for the measured 1.16-eV activation energy of the transformation kinetics of E4 (and E5) signals into  $E_{75}$  reported in Sec. IV A. The full mechanism is represented on Figs. 1(a)–1(d) sequence.

The above results suggest that the migration of neutral  $V_3$  should involve consecutive transformation sequences between FFC and PHR structures. Such a mechanism can be conceived by bringing an additional transformation coordinate  $Q_4$  to make a three-step ( $Q_2, Q_3, Q_4$ ) combination. This can be better understood by recalling Figs. 1(a)–1(d) and Fig. 11 where the relevant structures and MEP are represented. The minimum energy path for migration starts with the defect in the  $V_3[\text{FFC}^0]$  state [Fig. 1(d) and far right of Fig. 11(d)], reaches its halfway in the  $V_3[\text{PHR}^0]$  state [Fig. 1(a) and far left of Fig. 11(b)], and returns again to  $V_3[\text{FFC}]$  through a symmetry equivalent path. During the  $\text{FFC} \rightarrow C_2$  step, a pair of core Si atoms in structure  $V_3[\text{FFC}]$  dimerize by taking the place of two nearest neighboring vacant sites. The barrier to be surmounted is  $\Delta E_T[\text{FFC}^0 \rightarrow C_2^0] = 1.11$  eV high. The second step comprises a distortion of the  $\text{Si}_1\text{-Si}_2$  dimer, leading to a  $\Delta E_T[C_2^0 \rightarrow C_1^0] = -0.11$  eV relaxation from  $V_3[C_2^0]$  to the  $V_3[C_1^0]$  triclinic structure. Finally, in the third step, the tilted  $\text{Si}_1\text{-Si}_2$  dimer and  $\text{Si}_3$  make a correlated jump [in the opposite direction as represented by the arrows in Fig. 1(a)], and the spontaneous formation of the  $\text{Si}_2\text{-Si}_3$  bond is followed. The step barrier here is  $\Delta E_T[C_1^0 \rightarrow \text{PHR}^0] = 0.54$  eV, and comprises the limiting step of the whole migration mechanism with an overall barrier  $\Delta E_M^0 = 1.40$  eV high. This is in very good agreement with the experimental value of 1.47 eV obtained from the isochronal annealing studies reported above. Assuming a  $[111]$  defect orientation as depicted in Fig. 1(d), the first step has three possible products (ending with  $[1\bar{1}0]$ ,  $[10\bar{1}]$ , and  $[0\bar{1}1]$   $V_3[C_2]$  aligned structures, respectively). Each of these can transform to two  $V_3[\text{PHR}]$  alignments after taking steps 2 and 3. This means that half of the migration path provides a connection between a  $[111]$ -aligned FFC complex and the full family of six equivalent  $\langle 110 \rangle$ -aligned  $V_3[\text{PHR}]$  defects. As it was described above, the symmetry of the problem allows us to envisage up to four possible ( $Q_2, Q_3, Q_4$ ) transformations, so that each  $V_3[\text{PHR}]$  connects to the full family of four equivalent  $\langle 111 \rangle$ -aligned  $V_3[\text{FFC}]$  complexes as well. Hence, the proposed migration also combines reorientation, with  $V_3[\text{FFC}]$  jumping between neighboring  $\langle 111 \rangle$  hexagonal rings.

If the Fermi level is near the band edges,  $V_3$  is predicted to occur in the PHR form in the double plus or double minus charge states. According to Fig. 9 this is for  $E_c - E_F \lesssim 0.3$  and  $E_F - E_v \lesssim 0.1$ , respectively. Again, we calculated the MEP for one-step ( $Q_1$ ), two-step ( $Q_1, Q_2$ ), and three-step ( $Q_1, Q_2, Q_3$ ) migration paths, but in this case for charged supercells. MEP results are shown in Fig. 11 as open diamonds and inverted triangles that stand for the energy of  $V_3^{++}$  and  $V_3^{--}$ , respectively. For the  $Q_1$  transformation coordinate we found  $\Delta E_T[\text{PHR}^{++} \rightarrow C_{2h}^{++}] = 1.93$  eV and  $\Delta E_T[\text{PHR}^- \rightarrow C_{2h}^-] = 1.64$  eV, for  $Q_2$  we found  $\Delta E_T[\text{PHR}^{++} \rightarrow C_1^{++}] = 1.03$  eV and  $\Delta E_T[\text{PHR}^- \rightarrow C_1^-] = 1.03$  eV, for  $Q_3$  we have  $\Delta E_T[C_1^{++} \rightarrow C_2^{++}] = -0.08$  eV and

$\Delta E_T[C_1^- \rightarrow C_2^-] = -0.13$  eV, and finally for  $Q_4$  we have  $\Delta E_T[C_2^{++} \rightarrow \text{FFC}^{++}] = 0.37$  eV and  $\Delta E_T[C_2^- \rightarrow \text{FFC}^-] = 0.34$  eV. The saddle point is again along  $Q_2$ , but the half-way point of the migration mechanism is now at  $V_3[C_2]$ . This suggests that doubly positive and doubly negative trivacancies are able to migrate with barriers of  $\Delta E_M^{++}$  and  $\Delta E_M^{--}$  of about 1 eV, and therefore at lower temperatures than neutral  $V_3$ .

For the sake of completeness, we also report in Fig. 11 the MEP results for singly charged metastable trivacancies. Like for the neutral charge state, the saddle-point energies along  $Q_2$  and  $Q_4$  are distinguishable, and higher values occur along the  $V_3[\text{PHR}] \rightarrow V_3[C_1]$  step. By looking at Fig. 9 we conclude that migration in the plus or minus charge states is unlikely since these are thermodynamically unstable against neutral  $V_3^0$  [FFC]. Hence, immediately after irradiation, annealing of  $V_3^+[\text{PHR}]$  and  $V_3^-[\text{PHR}]$  defects is most likely to occur via the  $\text{PHR} \rightarrow \text{FFC}$  transformation with overall barriers of  $\Delta E_T[\text{PHR}^+ \rightarrow \text{FFC}^+] = 1.04$  eV and  $\Delta E_T[\text{PHR}^- \rightarrow \text{FFC}^-] = 1.14$  eV. While the transformation barrier for the plus charge was not measured, the barrier for the negative charge state is in excellent agreement with the 1.15-eV barrier from the annealing kinetics measurements.

## VI. CONCLUSIONS

The trivacancy is one of the most abundant defects in Si crystals irradiated with high energy particles (ions, neutrons, or electrons with  $E > 5$  MeV) and this center is responsible for the degradation of silicon detectors and bipolar transistors upon irradiation.<sup>11,15,19</sup> Understanding the details of the  $V_3$  electronic structure and dynamic properties is of crucial importance for improving the radiation hardness of Si detectors, which are widely used in high energy physics and medical radiation therapy.

We have studied the structure, electronic properties, transformation, and diffusion dynamics of the trivacancy in Si by combining density-functional modeling with DLTS, L-DLTS and annealing studies. Some results on the structural configurations and electronic properties of the  $V_3$  defect have been published by us earlier.<sup>15,16</sup> In the present paper the previously reported  $V_3$  structures and related electrical levels are confirmed, while our understanding of their electronic properties has been extended considerably. In short,  $V_3$  can occur in two forms, namely in FFC and PHR structures. The former is more stable in the neutral charge state, whereas  $V_3[\text{PHR}]$  has lower energy when it is charged from double minus to double plus charge states. The calculations were carried out by means of a density-functional code employing the local density approximation to the exchange-correlation energy.<sup>22,23</sup> Using this approach, electron chemical potential calculations are usually inaccurate and lead to a paradigmatic underestimation of the band gap,<sup>28</sup> but we mitigate this insufficiency by using the marker method to obtain the electrical levels. This method has been rather successful in the identification of many defect levels in semiconductors.<sup>26</sup>

Information on transformations between the configurations and diffusion of the  $V_3$  center has only been very briefly reported in previous experimental studies,<sup>11,15,16,44</sup> and there has been no consideration of these issues in theoretical



modeling studies. So, the focus of the present study has been on understanding the details of the transformations between different configurations of  $V_3$  and the mechanism of the long-range diffusion. This was achieved from experimental results based on careful measurements using high resolution Laplace DLTS on a wide range of test device structures and then finding atomic configurations with matching electronic and dynamic properties by means of *ab initio* calculations. The fruitfulness of such approach has been demonstrated previously by us in several reports, in which a number of electrically active point defects in Si and Ge have been identified.<sup>15,16,52–55</sup>

The transformation of the  $V_3$  defect from the PHR to the FFC configuration was monitored by following the decay of  $E_4/E_5$  and  $H_{193}/H_{106}$  DLTS signals ( $V_3$ [PHR] acceptor and donor levels) along with the growth of the  $E_{75}$  electron trap ( $V_3$ [FFC] acceptor level) during isothermal annealing treatments. The test diodes were annealed both under reverse bias and zero bias, and this enabled us to obtain PHR  $\rightarrow$  FFC transformation barriers of 1.16 and 1.145 eV for neutral and negatively charged defects, respectively. These are well accounted for by the respective calculated transformation barriers of 1.15 and 1.14 eV with initial, intermediate, and final structures depicted in Fig. 1.

At temperatures above 200 °C the intensity of the  $V_3$  related DLTS signals decreases in the irradiated diodes studied, and from isothermal annealing experiments on epi- and Cz-grown *n*-Si diodes we conclude that the defect anneals out with a barrier of 1.47 eV. This value is also well matched by the calculated 1.40-eV high barrier across a migration mechanism that involves consecutive FFC  $\leftrightarrow$  PHR reversible transformation steps. The decay kinetics of  $V_3$  upon annealing irradiated oxygen-rich Si samples at 230–270 °C correlates well with the formation of  $V_3O$  defects, indicating that  $V_3$  complexes migrate until they are trapped at interstitial oxygen impurities in the Si:O materials.

All the experimentally determined and calculated electronic and dynamical parameters of the  $V_3$  defect in silicon are listed in Table II. A very good agreement between the experimentally determined and calculated energies gives strong support to

TABLE II. Experimentally determined (Expt.) and calculated (Calc.) electronic and dynamical parameters of the trivacancy defect in silicon.

$V_3$ parameter	Expt. (eV)	Calc. (eV)
$E[\text{PHR}](=/-)$	$E_c - 0.359$	$E_c - 0.31$
$E[\text{PHR}](-/0)$	$E_c - 0.458$	$E_c - 0.43$
$E[\text{PHR}](0/+)$	$E_v + 0.193$	$E_v + 0.29$
$E[\text{PHR}](+/+)$	$E_v + 0.106$	$E_v + 0.15$
$E[\text{FFC}](-/0)$	$E_c - 0.075$	$E_c - 0.16$
$E(= / 0)$		$E_c - 0.27$
$E(0 / + +)$		$E_v + 0.11$
$E_T[\text{PHR}^0 \rightarrow \text{FFC}^0]$	1.16	1.15
$E_T[\text{PHR}^- \rightarrow \text{FFC}^-]$	1.145	1.14
$E_T[\text{PHR}^+ \rightarrow \text{FFC}^+]$		1.04
$\Delta E_M^0$	1.47	1.40
$\Delta E_M^{++}$		1.03
$\Delta E_M^-$		1.03

the microscopic model of the defect and mechanisms for its reconstructions and migration proposed by us. In consequence the identification of trivacancy in silicon is nearly complete. Perhaps the most intriguing question still to be answered is related to revealing the FFC  $\rightarrow$  PHR transformation mechanism upon injection of minority carriers. This phenomenon has been found to occur upon forward-bias-induced minority carrier injection into electron- and neutron-irradiated Si diodes,<sup>15,16,19</sup> but a detailed study of the process has not been carried out yet.

## ACKNOWLEDGMENTS

J.C. thanks the NanoTP Cost Action MP0901 for funding and the Fundação para a Ciência e a Tecnologia, Portugal (FCT) under Grant No. PEst-C/CTM/LA0025/2011. The University of Manchester team thanks the United Kingdom Engineering and Physical Sciences Research Council for partial funding of this work under a Platform Grant.

\*jose.coutinho@ua.pt

<sup>1</sup>A. Dierlamm, *Nuclear Instr. Meth. Phys. Res. A* **624**, 396 (2010).

<sup>2</sup>J. Xu, E. G. Roth, O. W. Holland, A. P. Mills, and R. Suzuki, *Appl. Phys. Lett.* **74**, 997 (1999).

<sup>3</sup>H. Wong, N. W. Cheung, P. K. Chu, J. Liu, and J. W. Mayer, *Appl. Phys. Lett.* **52**, 1023 (1988).

<sup>4</sup>M. Nisenoff and H. Y. Fan, *Phys. Rev.* **128**, 1605 (1962).

<sup>5</sup>W. Jung and G. S. Newell, *Phys. Rev.* **132**, 648 (1963).

<sup>6</sup>K. L. Brower, *Radiat. Eff.* **8**, 213 (1971).

<sup>7</sup>Y. H. Lee, Y. M. Kim, and J. W. Corbett, *Radiat. Eff.* **15**, 77 (1972).

<sup>8</sup>Y.-H. Lee and J. W. Corbett, *Phys. Rev. B* **9**, 4351 (1974).

<sup>9</sup>B. Hourahine, R. Jones, A. N. Safonov, S. Öberg, P. R. Briddon, and S. K. Estreicher, *Phys. Rev. B* **61**, 12594 (2000).

<sup>10</sup>A. S. Kaminski, *JETP Lett.* **73**, 28 (2001).

<sup>11</sup>M. Ahmed, S. J. Watts, J. Matheson, and A. Holmes-Siedle, *Nuclear Instr. Meth. Phys. Res. A* **457**, 588 (2001).

<sup>12</sup>J. L. Hastings, S. K. Estreicher, and P. A. Fedders, *Phys. Rev. B* **56**, 10215 (1997).

<sup>13</sup>D. J. Chadi and K. J. Chang, *Phys. Rev. B* **38**, 1523 (1988).

<sup>14</sup>D. V. Makhov and L. J. Lewis, *Phys. Rev. Lett.* **92**, 255504 (2004).

<sup>15</sup>V. P. Markevich, A. R. Peaker, S. B. Lastovskii, L. I. Murin, J. Coutinho, V. J. B. Torres, P. R. Briddon, L. Dobaczewski, E. V. Monakhov, and B. G. Svensson, *Phys. Rev. B* **80**, 235207 (2009).

<sup>16</sup>V. P. Markevich, A. R. Peaker, B. Hamilton, S. B. Lastovskii, L. I. Murin, J. Coutinho, V. J. B. Torres, L. Dobaczewski, and B. G. Svensson, *Phys. Status Solidi A* **208**, 568 (2011).

<sup>17</sup>L. I. Murin, B. G. Svensson, J. L. Lindström, V. P. Markevich, and C. A. Londos, *Physica B* **404**, 4568 (2009).

<sup>18</sup>M. Moll, H. Feick, E. Fretwurst, G. Lindström, and C. Schütze, *Nuclear Instr. Meth. Phys. Res. A* **388**, 335 (1997).

<sup>19</sup>R. M. Fleming, C. H. Seager, D. V. Lang, E. Bielejec, and J. M. Campbell, *Appl. Phys. Lett.* **90**, 172105 (2007).



- <sup>20</sup>L. Dobaczewski, A. R. Peaker, and K. Bonde Nielsen, *J. Appl. Phys.* **96**, 4689 (2004).
- <sup>21</sup>M. Mikelsen, E. V. Monakhov, G. Alfieri, B. S. Avset, and B. G. Svensson, *Phys. Rev. B* **72**, 195207 (2005).
- <sup>22</sup>P. Briddon and R. Jones, *Phys. Status Solidi B* **217**, 131 (2000).
- <sup>23</sup>M. J. Rayson and P. R. Briddon, *Comp. Phys. Commun.* **178**, 128 (2008).
- <sup>24</sup>J. P. Perdew and Y. Wang, *Phys. Rev. B* **45**, 13244 (1992).
- <sup>25</sup>C. Hartwigsen, S. Goedecker, and J. Hutter, *Phys. Rev. B* **58**, 3641 (1998).
- <sup>26</sup>J. P. Goss, M. J. Shaw, and P. R. Briddon, in *Theory of Defects in Semiconductors*, Topics in Applied Physics, Vol. 104, edited by D. A. Drabold and S. K. Estreicher (Springer, Berlin, 2007), Chap. 3, p. 69.
- <sup>27</sup>P. J. Mohr and B. N. Taylor, *Rev. Mod. Phys.* **72**, 351 (2000).
- <sup>28</sup>R. W. Godby, M. Schlüter, and L. J. Sham, *Phys. Rev. Lett.* **56**, 2415 (1986).
- <sup>29</sup>S. M. Sze, *Physics of Semiconductor Devices*, 2nd ed. (John Wiley & Sons, New York, 1981).
- <sup>30</sup>S. Lany and A. Zunger, *Phys. Rev. B* **78**, 235104 (2008).
- <sup>31</sup>G. Makov and M. C. Payne, *Phys. Rev. B* **51**, 4014 (1995).
- <sup>32</sup>H. Nozaki and S. Itoh, *Phys. Rev. E* **62**, 1390 (2000).
- <sup>33</sup>C. G. Van de Walle and R. M. Martin, *Phys. Rev. B* **35**, 8154 (1987).
- <sup>34</sup>A. Resende, R. Jones, S. Öberg, and P. R. Briddon, *Phys. Rev. Lett.* **82**, 2111 (1999).
- <sup>35</sup>J. Coutinho, V. J. B. Torres, R. Jones, and P. R. Briddon, *Phys. Rev. B* **67**, 035205 (2003).
- <sup>36</sup>J.-W. Jeong and A. Oshiyama, *Phys. Rev. B* **64**, 235204 (2001).
- <sup>37</sup>V. P. Markevich, A. R. Peaker, S. B. Lastovskii, L. I. Murin, J. Coutinho, A. V. Markevich, V. J. B. Torres, P. R. Briddon, L. Dobaczewski, E. V. Monakhov, and B. G. Svensson, *Physica B* **404**, 4565 (2009).
- <sup>38</sup>G. Henkelman, B. P. Uberuaga, and H. Jónsson, *J. Chem. Phys.* **113**, 9901 (2000).
- <sup>39</sup>G. Henkelman and H. Jónsson, *J. Chem. Phys.* **113**, 9978 (2000).
- <sup>40</sup>A. Carvalho, R. Jones, M. Sanati, S. K. Estreicher, J. Coutinho, and P. R. Briddon, *Phys. Rev. B* **73**, 245210 (2006).
- <sup>41</sup>A. Carvalho, R. Jones, C. Janke, J. P. Goss, P. R. Briddon, J. Coutinho, and S. Öberg, *Phys. Rev. Lett.* **99**, 175502 (2007).
- <sup>42</sup>M. Moll, E. Fretwurst, M. Kuhnke, and G. Lindström, *Nuclear Instr. Meth. Phys. Res. B* **186**, 100 (2002).
- <sup>43</sup>J. H. Bleka, E. V. Monakhov, B. G. Svensson, and B. S. Avset, *Phys. Rev. B* **76**, 233204 (2007).
- <sup>44</sup>J. H. Bleka, L. Murin, E. V. Monakhov, B. S. Avset, and B. G. Svensson, *Appl. Phys. Lett.* **92**, 132102 (2008).
- <sup>45</sup>L. C. Kimmerling, H. M. DeAngelis, and J. W. Diebold, *Solid State Commun.* **16**, 171 (1975).
- <sup>46</sup>V. P. Markevich, A. R. Peaker, S. B. Lastovskii, L. I. Murin, and J. L. Lindström, *J. Phys.: Condens. Matter* **15**, S2779 (2003).
- <sup>47</sup>G. S. Hwang and W. A. Goddard III, *Phys. Rev. B* **65**, 233205 (2002).
- <sup>48</sup>J. A. Kubby and J. J. Boland, *Surf. Sci. Rep.* **26**, 61 (1996).
- <sup>49</sup>D. J. Chadi, *Phys. Rev. Lett.* **43**, 43 (1979).
- <sup>50</sup>S. Ögüt and J. R. Chelikowsky, *Phys. Rev. Lett.* **83**, 3852 (1999).
- <sup>51</sup>T. E. M. Staab, A. Sieck, M. Haugk, M. J. Puska, T. Frauenheim, and H. S. Leipner, *Phys. Rev. B* **65**, 115210 (2002).
- <sup>52</sup>V. P. Markevich, A. R. Peaker, B. Hamilton, V. V. Litvinov, Y. M. Pokotilo, S. B. Lastovskii, J. Coutinho, A. Carvalho, M. J. Rayson, and P. R. Briddon, *J. Appl. Phys.* **109**, 083705 (2011).
- <sup>53</sup>L. I. Murin, E. A. Tolkacheva, V. P. Markevich, A. R. Peaker, B. Hamilton, E. Monakhov, B. G. Svensson, J. L. Lindström, P. Santos, J. Coutinho, and A. Carvalho, *Appl. Phys. Lett.* **98**, 182101 (2011).
- <sup>54</sup>V. P. Markevich, A. R. Peaker, J. Coutinho, R. Jones, V. J. B. Torres, S. Öberg, P. R. Briddon, L. I. Murin, L. Dobaczewski, and N. V. Abrosimov, *Phys. Rev. B* **69**, 125218 (2004).
- <sup>55</sup>A. Carvalho, R. Jones, V. J. B. Torres, J. Coutinho, V. P. Markevich, S. Öberg, and P. R. Briddon, *J. Mater. Sci.: Mater. Electron.* **18**, 781 (2007).